crystals

MDPI

Article

Influence of Polymeric Blends on Bioceramics of Hydroxyapatite

Eduardo da Silva Gomes [1], Antônia Millena de Oliveira Lima [1,2], Sílvia Rodrigues Gavinho [3], Manuel Pedro Fernandes Graça [3,*], Susana Devesa [4,*] and Ana Angélica Mathias Macêdo [1]

[1] Federal Institute of Maranhão (IFMA)—Campus Imperatriz, Research Laboratory, Imperatriz 65919-050, Brazil; eduardo.anm2@gmail.com (E.d.S.G.); amillenalima@hotmail.com (A.M.d.O.L.); anaangellica@yahoo.com.br (A.A.M.M.)
[2] Foundation for Research and Scientific and Technological Development of Maranhão, (FAPEMA), São Luís 65075-340, Maranhão, Brazil
[3] I3N and Physics Department, University of Aveiro, 3810-193 Aveiro, Portugal; silviagavinho@ua.pt
[4] CEMMPRE, Centre for Mechanical Engineering, Materials and Processes, Department of Mechanical Engineering, University of Coimbra, Rua Luís Reis Santos, 3030-788 Coimbra, Portugal
* Correspondence: mpfg@ua.pt (M.P.F.G.); susana_devesa@hotmail.com (S.D.)

Abstract: Bioceramics are used to repair, rebuild, and replace parts of the human body, e.g., bones, joints and teeth, in the form of powder, coatings or prostheses. The synthetic hydroxyapatite [$Ca_{10}(PO_4)_6(OH)_2$ (HAP)] based on calcium phosphate has been widely used in the medical and dental areas due to the chemical similarity with the inorganic component of human bone tissue. In this work, hydroxyapatite nanocrystalline powders were synthesized by the solid-state reaction method and sintered with a galactomannan and chitosan blend. The bioceramics studied were prepared from 70%, 80% and 90% of hydroxyapatite with 30%, 20% and 10% of galactomannan and chitosan blends, respectively. The influence of the blend content on the bioceramics was investigated through structural, vibrational, thermal, morphological and dielectric characterizations. It was observed that the increase in the blend percentage promoted an increase in the grain size, which was followed by a decrease in the density and hardness of the samples. The sample with a higher amount of polymeric blend also presented a higher dielectric constant and higher losses.

Keywords: hydroxyapatite; galactomannan; chitosan; polymeric blend; bioceramics

Citation: Gomes, E.d.S.; Lima, A.M.d.O.; Gavinho, S.R.; Graça, M.P.F.; Devesa, S.; Macêdo, A.A.M. Influence of Polymeric Blends on Bioceramics of Hydroxyapatite. *Crystals* **2023**, *13*, 1429. https://doi.org/10.3390/cryst13101429

Academic Editor: Michele Iafisco

Received: 1 August 2023
Revised: 13 September 2023
Accepted: 23 September 2023
Published: 26 September 2023

1. Introduction

The various pathologies that affect the bone structure, such as osteoporosis and loss of bone mass, encouraged the search for synthetic materials that facilitate bone repair, aiming for the rapid restoration of physiological functions [1,2]. Among these materials, bioceramics are used to repair, rebuild and replace parts of the human body, e.g., bones, joints, teeth and others, in the form of powder or coatings for prostheses [3,4].

The biomineral phase, based on calcium phosphates, is the main constituent of calcified tissues (bone, enamel and dentin), which is present in human bone in a composition range of about 65–70%, whereas the water content is in the range of 5–8% and the organic phase constitutes the remaining content [5].

Calcium phosphate salts, such as the synthetic hydroxyapatite $Ca_{10}(PO_4)_6(OH)_2$ (HAP), have been widely used in the orthopedic and dental fields since they have chemical similarity with the inorganic component of human bone tissue and high stability in the presence of biological fluids. As a consequence, HAP has osteoconductivity, biocompatibility and bioactivity properties, i.e., the ability to form chemical bonds with neighboring hard tissues after implantation [5–11].

The HAP has been studied in the form of powder and coating, such as nano or microparticles [12,13], with its synthesis being reported by different wet and dry methods,

e.g., precipitation in aqueous solutions, sol–gel processes, high-energy grinding, etc. [14–19]. The various techniques used for the synthesis of HAP infer different characteristics that influence, for example, its orthopedic and dental application [4,9].

In the wet synthesis processes, since aqueous solutions are used, the by-product is mainly water, producing, generally, nano-sized and homogeneous powders. Moreover, there is a very low probability of contamination. However, disadvantages, such as the inherent difficulty in controlling the exact stoichiometric composition of the product and the long time required to obtain HAP powders, culminate in poor reproducibility and high processing costs.

In the dry synthesis processes, i.e., processes that do not require solvents, there is no need for specific controllable conditions, leading to high reproducibility and low cost. However, the risk of contamination can be increased during the milling process, with most of the dry processes having difficulty producing nano-sized HAP powders [20–22].

The HAP obtained at low temperatures presents low crystallinity being a fragile material. At high temperatures (above 900 °C), HAP presents good crystallinity and can produce a more resistant material and is also easy to handle [23].

HAP can be used as a biomaterial and as ion exchangers, adsorbents and catalysts; however, one of the most effective uses of HAP is as a hybrid material with biopolymers [24,25], having, as an example, its joint use with collagen, chitosan and chitin, synthesized by various methods, including precipitation, electrochemical deposition and blending, i.e., a biomimetic process with simulation of the biological fluid [26–33]. These biopolymers end up inferring changes in the properties of HAP, particularly the dielectric, vibrational, morphological and optical properties [34–36].

In this context, chitosan, a polycationic linear biopolymer, amino derived from the partial or total deacetylation process of the chitin [37], with a structure formed by the repetition of N-acetyl-D-glucosamine or 2-acetamido-2-deoxy-D-glucose units in diluted β(1→4) connections [38], contains numerous advantages, e.g., displaying high biodegradability, high biocompatibility, chemical inertia and good film-forming properties [39,40].

Galactomannan, a polysaccharide present in the seed endosperm of a variety of leguminous plants, consists of linear chains of (1–4) linked β-D-mannopyranosyl residues, most of which are substituted with (1–6) linked α-D-galactopyranosyl side-chain residues, with the ratio of mannose to galactose depending on the plant source and the method of extraction. These compounds have been studied in binary mixtures with other polysaccharides due to their gel formation ability, rheological properties and applicability in several systems [41–44].

The biopolymers mentioned, once added to the synthesis of HAP, can lead to changes in its properties. Therefore, in this study, HAP nanocrystalline powders were synthesized and sintered with a galactomannan and chitosan blend. The influence of the blend on the bioceramic was investigated through structural, vibrational, thermal, dielectric and morphological characterizations.

2. Materials and Methods

2.1. Bioceramics Preparation

The sample preparation consisted of six steps: synthesis of hydroxyapatite, galactomannan extraction and solution preparation, chitosan solution preparation, polymeric blend preparation and, finally, the production of the bioceramics composed of hydroxyapatite and the polymeric blend.

The synthesis of HAP was performed by the high-energy method, using stoichiometric amounts of calcium hydroxide, $Ca(OH)_2$ (Vetec, 97%), and calcium hydrogen phosphate, $CaHPO_4$ (Aldrich, St. Louis, MO, USA, 99%), according to the chemical reaction presented in Equation (1):

$$4Ca(OH)_2 + 6CaHPO_4 \rightarrow Ca_{10}(PO_4)_6(OH)_2 + 6H_2O \quad (1)$$

The starting materials were ground in a Fritsch Pulverisette 6 planetary ball mill. During grinding, air-sealed stainless steel bowls and balls were used, with a rotation speed of 370 rpm. To avoid excessive heat, the synthesis was performed in 30 min stages with 10 min pauses, with a total duration of 20 h.

The crude galactomannan was extracted from the seeds of *Adenanthera pavonina* L. The endosperms were obtained after heating the seeds in boiling distilled water for 20 min with enzymatic inactivation, followed by swelling for 12 h. The seed coats were removed and then the endosperms were separated from the embryo and stored under refrigeration [34].

The galactomannan solution (GP) was obtained by the solubilization of the endosperms at room temperature in a 0.1% acetic acid solution (pH = 3.0) for 1 h under mechanical agitation. The solution was centrifuged at 14,560× *g* (10,000 rpm) for 1 h, and the dry matter of the suspension was obtained by heating it at 100 °C until a constant weight was reached. The resulting solution was taken to a final concentration of 10 mg/g.

The chitosan solution (CP) was obtained by the solubilization of the chitosan powder (Sigma/Aldrich, St. Louis, MO, USA,) at room temperature in 0.1% acetic acid solution (pH = 3.0) for 24 h under mechanical agitation. The solution was centrifuged at 14,560× *g* for 1 h, with the resulting solution taken to a final concentration of 5 mg/g.

The polymeric blend of galactomannan and chitosan (GC) was prepared from the homogenization of GP (10 mg/g) and CP (5 mg/g) solutions, obtained by agitation at room temperature, centrifuged at 582 *g* for 20 min and stored under refrigeration until use.

Figure 1 shows the representative flowchart of GC blend preparation and the processes that preceded it.

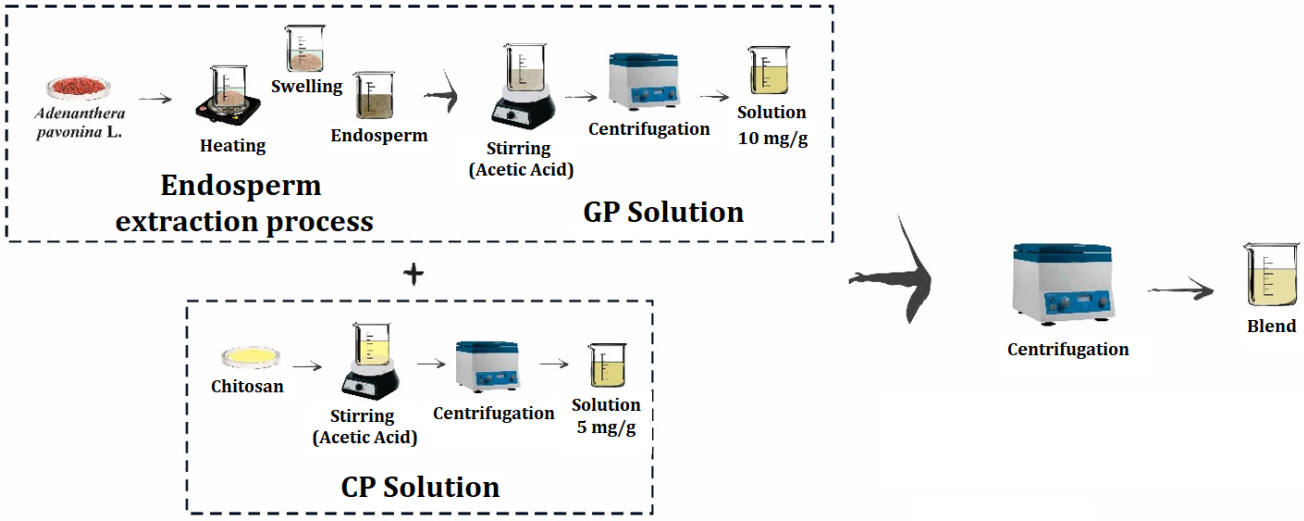

Figure 1. Representative flowchart of the extraction of galactomannan and preparation processes of the GP and CP solutions as well as the synthesis of the GC blend.

Finally, the bioceramics were prepared from 70%, 80% and 90% of HAP nanocrystalline powder with 30%, 20% and 10% of GC blends, respectively, and categorized as follows: H70GC30, H80GC20 and H90GC10. The resulting powders were molded into cylindrical pellets that were 10 mm in diameter and 1 mm in height by cold uniaxial pressing (260 MPa) in a hydraulic press. The samples were then sintered at 900 °C for 5 h at a heating rate of 5 °C/min.

Figure 2 shows the representative flowchart of the bioceramics preparation process.

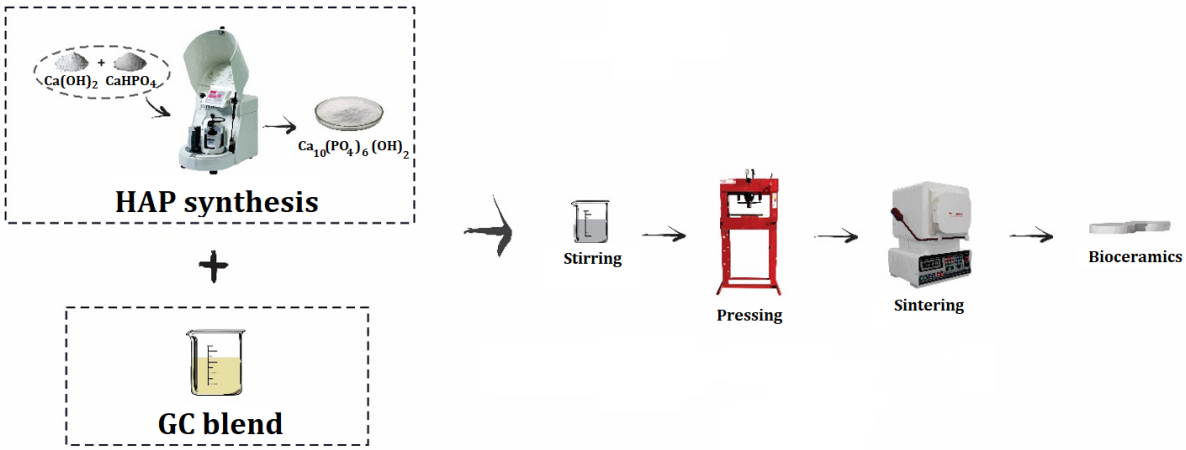

Figure 2. Representative flowchart of the H70GC30, H80GC20 and H90GC10 bioceramics preparation.

2.2. Bioceramics Characterization

X-ray diffraction (XRD) patterns were determined by a Rigaku DMAXB diffractometer configured in a Bragg–Brentano geometry with Cu Kα radiation (40 kV and 25 mA). The analyses were performed at room temperature (27 °C) with an angular interval of 10–70° (2θ) at a rate of 1°/min. The XRD patterns were analyzed by the Rietveld refinement method [45]. The quantitative analysis of the Rietveld refinement was performed using the BGMN software with the Profex interface [46]. This method consists of minimizing the sum of squares of the difference between the intensities observed and calculated for each point of the powder diffraction pattern (Equation (2)).

$$M = \sum_i w_i \left(I_{OBS_i} - I_{CALC_i}\right)^2 \quad (2)$$

where M is the minimum residue, I_{OBS_i} is the intensity of the experimental diffraction pattern in the i-point, I_{CALC_i} is the intensity of the theoretical diffraction pattern in the i-point and w_i is the weight for each measured point [18]. To evaluate the quality of the adjustment, quantitative factors that require reliable data are used, and among them, we can define the standard weight residue, R_{WP}, and the expected residue, R_{exp}, presented in Equations (3) and (4).

$$R_{WP} = \left[\frac{\sum_i w_i \left(I_{OBS_i} - I_{CALC_i}\right)^2}{\sum_i w_i \left(I_{OBS_i}\right)^2}\right]^{\frac{1}{2}} \quad (3)$$

$$R_{exp} = \left(\frac{N - P}{\sum_i w_i \left(I_{OBS_i}\right)^2}\right)^{\frac{1}{2}} \quad (4)$$

where N is the total number of observed points and P is the number of fitted parameters. From the mathematical point of view, the factor with the greatest statistical significance to be evaluated is the R_{WP} because it depends on the minimum residue M. Another important factor is S, also called the goodness of fit (Equation (5)), and should be close to 1.0 at the end of the refinement process.

$$S = \frac{R_{WP}}{R_{exp}} \quad (5)$$

The size of the crystallite, L_C, can be estimated from the Scherrer formula, presented in Equation (6), and using the peaks obtained from X-ray diffraction.

$$L_C = \frac{k\lambda}{\beta \cos\theta} \quad (6)$$

where k is the constant that depends on the morphology and direction of the material network (and is equal to 0.9), λ is the wavelength of X-rays, β is the width at half height of the diffracted peak (FWHM) and θ is the Bragg angle of the corresponding diffracted peak [47]. The percentage degree of crystallinity (X_C) was determined using Equation (7) [48].

$$X_C = 100 \times \frac{I_{exp} - I_{back}}{I_{exp}} \quad (7)$$

where I_{exp} refers to the total integrated area of the experimental pattern obtained by X-ray diffraction and I_{back} is the integral area of the baseline that corresponds to the amorphous region.

The Fourier transform infrared (FTIR) spectra of hydroxyapatite and hydroxyapatite samples with polymeric blends were obtained using KBr, measured in the region between 400 and 4000 cm^{-1}, using the SHIMATZU FTIR-283B spectrometer.

The experimental density was measured by Archimedes' principle using a pycnometer.

The thermogravimetry (TG) analyses were performed using the SHIMADZU TGA 50H thermal analyzer. The samples were heated in an inert atmosphere of nitrogen gas at a heating rate of 10 °C/min. The differential scanning calorimetry (DSC) studies were performed in a Shimadzu DSC50 thermal analyzer, with utilization of the same heating rate.

To perform scanning electron microscopy (SEM), the samples were coated with gold and analyzed in a Phillips XL-30 operating with primary electron groups limited between 12 and 20 KeV. The average grain size was estimated from the obtained micrographs.

To evaluate the hardness of the samples, a SHIMADZU HMV2 microdurometer was used, and was equipped with a standard Vickers microhardness tester, upon which a load of 920.7 mN was applied for 20 s. We then performed 10 indentations in each sample, with 10 mm in diameter and 1 mm in thickness. The hardness is the mechanical property used to know the strength of the material, and it is related to the material's density and morphology. The Vickers microhardness tester consists of a pyramidal diamond penetrator that is forced against the specimen. The Vickers hardness, H_V, of each sample was determined according to Equation (8).

$$H_V = \frac{L}{2d^2} \quad (8)$$

where d is the average length of the indentation diagonal, expressed in meters, and L the indentation load, in Newton [49,50].

The dielectric measurements of the GC blend and the bioceramics H70GC30, H80GC20 and H90GC10 were performed using the Solartron 1260 Impedance Analyzer in the frequency range from 1 Hz to 30 MHz at room temperature (27 °C). The real part of the dielectric permittivity, ε', was calculated from the measured capacitance, C, of the samples, and is given by Equation (9).

$$\varepsilon' = \frac{Cd}{\varepsilon_0 A} \quad (9)$$

where d is sample thickness, A is the surface area of the electrode and ε_0 is the vacuum permittivity (8,851,014 $\times$ 10^{-12} F/m).

The complex part of the dielectric permittivity, ε'', was obtained from the resistance, R, of the samples by applying Expression (10):

$$\varepsilon'' = \frac{d}{R\omega\varepsilon_0 A} \quad (10)$$

The real and complex parts of the dielectric permittivity can be related by the tangent loss, $tan\delta$, which is given by Equation (11).

$$tan\delta = \frac{\varepsilon''}{\varepsilon'} \quad (11)$$

The ε' measures the ability of a dielectric to store energy and relates to the polarization that occurs in the material subject to an electric field. The ability of a material to convert electromagnetic energy into heat is measured by the ε'' [51–56].

3. Results

3.1. XRD and Rietveld Refinement

The structure of the HAP (sintered at 900 °C for 5 h with a heating rate of 5 °C/min) was determined by XRD. Figure 3a shows the XRD patterns and the ICSD 429,746 profile [57]. It is observed that the HAP assumes all the characteristic peaks of the hexagonal phase of hydroxyapatite, not presenting peaks that could be assigned to secondary phases. The crystallite size, L_C, and the percentage degree of crystallinity, X_C, of the sintered HAP, obtained using Equations (6) and (7), are (30.45 ± 0.7) nm and 37.52%, respectively, and are depicted in Table 1. Silva et al. [58], when synthesizing hydroxyapatite samples by high-energy mechanical grinding, obtained an average crystallite size between 22 and 39 nm, showing good agreement with this work.

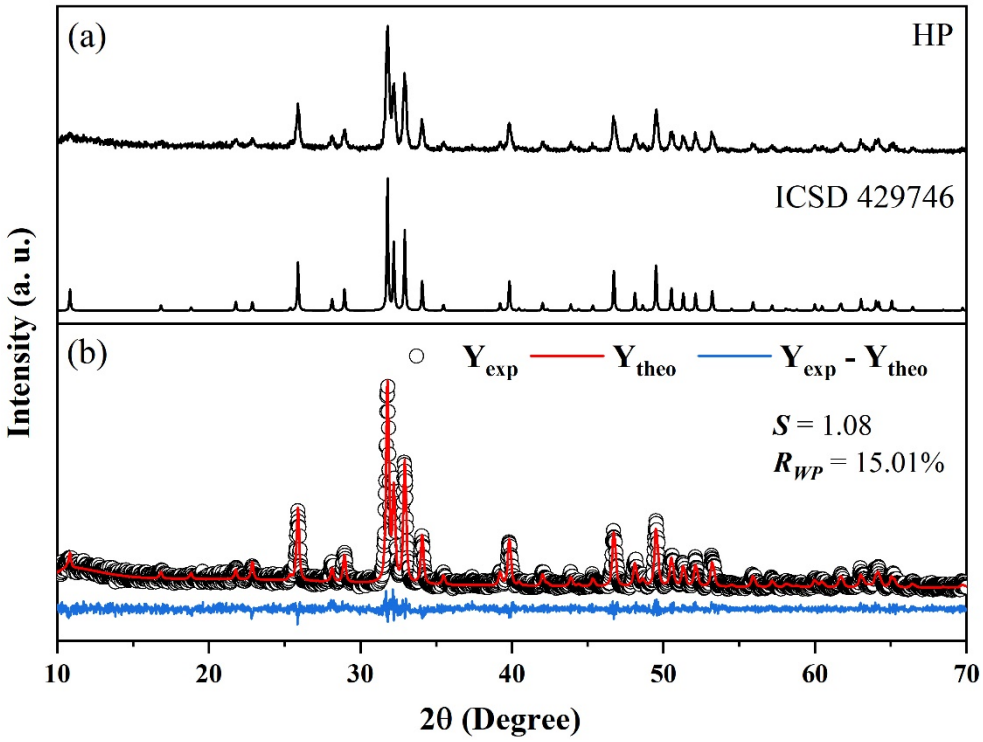

Figure 3. (**a**) XRD pattern of the HAP sintered and ICSD 429746. (**b**) Rietveld refinement of the HAP spectrum.

Table 1. Structural parameters obtained through the XRD pattern and Rietveld refinement.

Sample	Lattice Parameter			R_{WP} (%)	S	ρ (g/cm^3)	L_C (nm)	X_C (%)
	a = b (Å)	c (Å)	V (Å^3)					
HAP	9.4204 (7)	6.8823 (5)	528.9358 (5)	15.01	1.08	3.147	30.45 ± 0.7	37.52

With the Rietveld refinement, a quantitative analysis of the crystalline phase of HAP was performed. Figure 3b confirms that the sample presents 100% of the $Ca_{10}(PO_4)_6(OH)_2$ phase, with a hexagonal structure characteristic of the space group $P6_3/m$, and the network parameters and density presented in Table 1. The results found are aligned with the values

previously reported [57,58]. The R_{WP} and S values, obtained using Equations (3)–(5), are satisfactory since they are within their typical range [19,59].

3.2. Infrared Spectroscopy

The FTIR spectrum for the HAP sample, measured in the region ranging from 2000 cm^{-1} to 400 cm^{-1}, is displayed in Figure 4. The characteristic bands, assigned to the functional groups phosphate (PO_4^{3-}), carbonate (CO_3^{2-}) and hydroxyl (OH^-) can be identified: the bands at 569 cm^{-1}, 603 cm^{-1}, 968 cm^{-1}, 1043 cm^{-1} and 1093 cm^{-1} can be attributed to the PO_4^{3-} ion; the bands at 1419 cm^{-1} and 1469 cm^{-1} arise from vibrations of the CO_3^{2-} ions; and vibrations associated to OH^- are observed at 630 cm^{-1} and 1649 cm^{-1}. The band at 1649 cm^{-1} corresponds to free OH^-, attributed to symmetric deformation in the molecule of H_2O adsorbed in the synthesis process. The bands at 1469 cm^{-1} and 1419 cm^{-1} are assigned to the asymmetric stretching vibration of carbonate ions. The bands at 1093 cm^{-1} and 1043 cm^{-1} may be ascribed to the triply degenerated ν_3 anti-symmetric stretching of the P–O band, and the 968 cm^{-1} band can be due to the ν_1 non-degenerated symmetric stretching of the P–O bond. The band refers to the oscillation mode of the OH^- ions, and the band of the P-OH bond corresponding to the water adsorbed on the surface is visible at 630 cm^{-1}. Finally, the bands at 603 cm^{-1} and 569 cm^{-1} can be attributed to the triply degenerated ν_4 vibration of the O–P–O bond, and the band at 478 cm^{-1} may be related to the doubly degenerated ν_2 O–P–O bending.

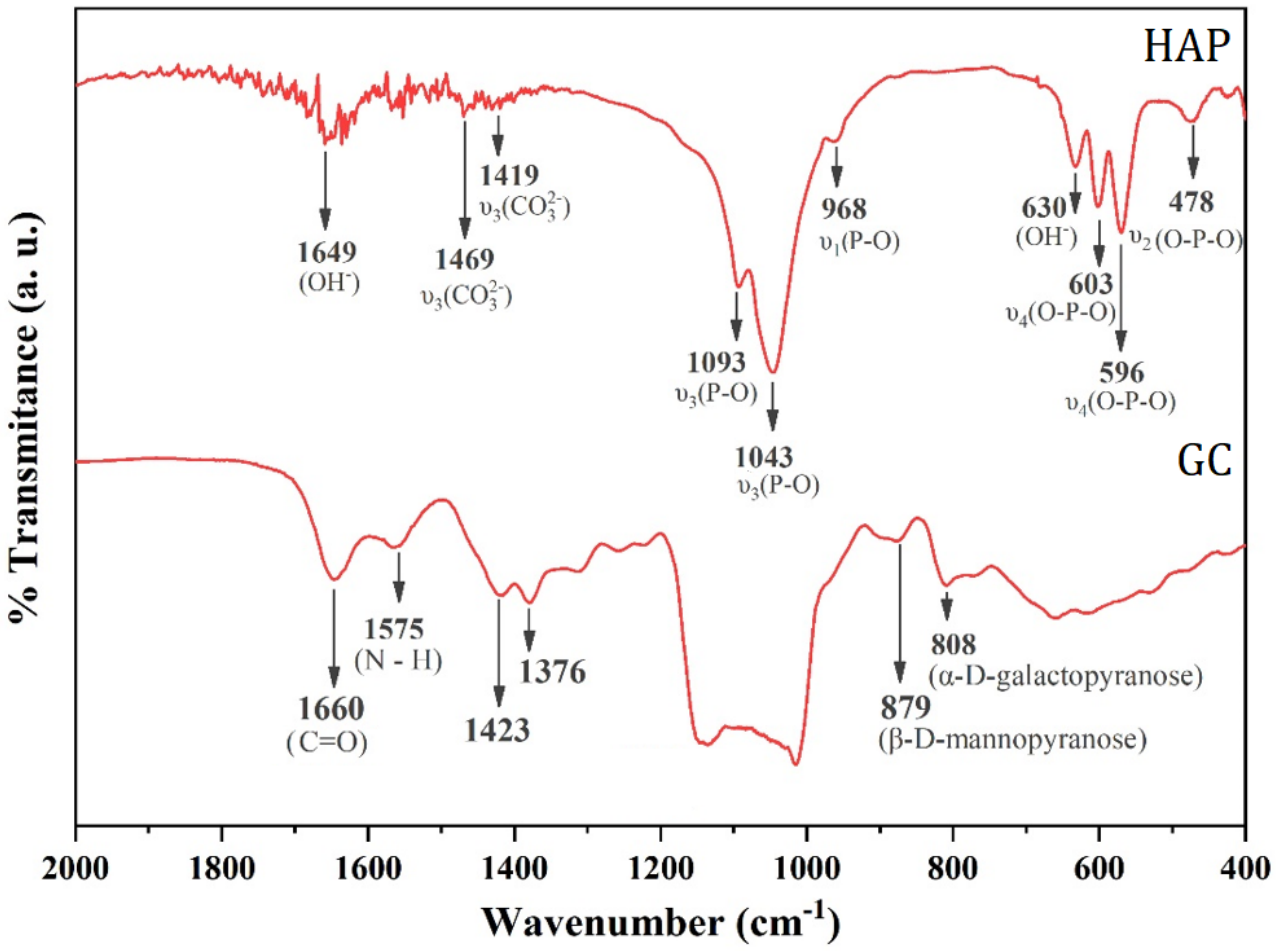

Figure 4. Infrared spectra of HAP and GC blend measured in the range of 400 to 2000 cm^{-1}.

The results obtained are in agreement with the literature [15,16,47,60–64] and the observed bands and their corresponding assignments can be consulted in Table 2.

Table 2. FTIR bands with corresponding vibrations for HAP and GC.

Bands	Wavenumber (cm^{-1})	
	HAP	**GC**
υ_2 (O-P-O)	478	-
υ_4 (O-P-O)	569	-
υ_4 (O-P-O)	603	-
OH^-	630	-
α–D–galactopyranose	-	808
β–D–mannopyranose	-	879
υ_1 (P-O)	968	-
CH_3	-	1139
υ_3 (P-O)	1043	-
υ_3 (P-O)	1093	-
C-O-C stretching vibration		1000 to 1110
Symmetric deformations of groups CH_2 and COH	-	1350 to 1450
υ_3 (CO_3^{2-})	1419	-
υ_3 (CO_3^{2-})	1469	-
N−H	-	1575
OH^-	1649	-
C=O	-	1660

The FTIR spectrum of the GC blend, measured in the region from 2000 cm^{-1} to 400 cm^{-1}, is also depicted in Figure 4. The bands at 808 cm^{-1} and 879 cm^{-1} indicate the presence of α–D–galactopyranose and β–D–mannopyranose units, respectively, and, at 1014 cm^{-1}, a common band of polysaccharides is also present. It is noteworthy that the band between 1000 and 1110 cm^{-1} is attributed to C-O-C stretching vibration and, in the region from 1350 to 1450 cm^{-1}, the bands correspond to the symmetrical deformations of the CH_2 and COH groups [65–68].

According to [69], these spectra can be influenced by parameters such as the deacetylation percentage or crystallinity. The IR spectra of chitosan, which is essentially produced from chitin by a deacetylation reaction, corresponds to a convolution of specific signals for carbohydrates and absorption due to amine and amide functions. Therefore, the band at 1575 cm^{-1} arises from the peptide bond vibration amide II and can be ascribed to the N–H stretching vibrations, while the 1660 cm^{-1} band is assigned to the stretching vibrations of C=O due to the peptide bond vibration amide I [69–73].

The analysis of the IR of the bioceramics H70GC30, H80GC20 and H90GC10 showed the same absorptions of HAP.

3.3. Thermal Analysis

To study the thermal behavior of HAP and the GC blend, thermogravimetry and differential scanning calorimetry measurements were performed and are depicted in Figures 5 and 6.

The TG curve shows a three-stage weight loss at the temperature ranges of 20–100, 100–300 and 300–500 °C, approximately.

In the first stage, the weight loss is due to the evaporation of adsorbed water [72,73]. The presence of water, physically adsorbed in the synthesis process of HAP, was already discussed in the infrared spectrum analysis. The second stage shows weight loss due to the release of adsorbed and lattice water, which is in accordance with the findings of Tõnsuaadu et al. [74], which stated that the lattice water is irreversibly lost between 200 and 400 °C. The third stage may represent the loss of water from decomposition, which means that in the present case, the removal of water molecules starts at lower temperatures when compared to the literature. According to Tõnsuaadu et al. [75], the dehydroxylation of HAP with the removal of water molecules in the air atmosphere starts at 900 °C. However, Bulina et al. [73] reported that this process probably starts at a lower temperature, specifically 600 °C, and Mandal et al. [72] considered the temperature of 780 °C to be the beginning

point of the dihydroxylation process. Such a temperature discrepancy should be attributed to the differences between samples and the experimental method [75]. Above 500 °C, HAP is thermally stable since stoichiometric hydroxyapatite with a Ca/P ratio of 1.67 is stable up to 1200 °C [76].

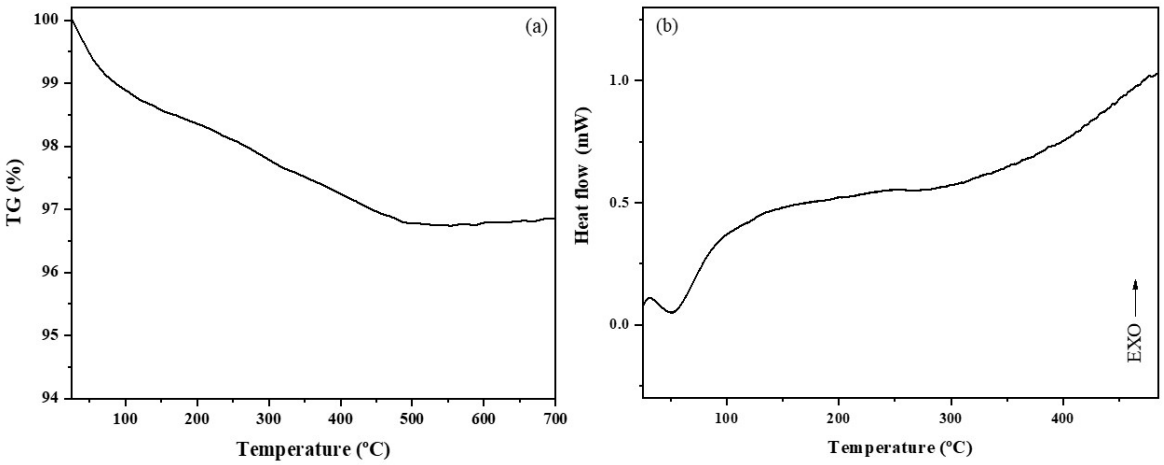

Figure 5. Thermal stability curves of HAP: (**a**) TG and (**b**) DSC.

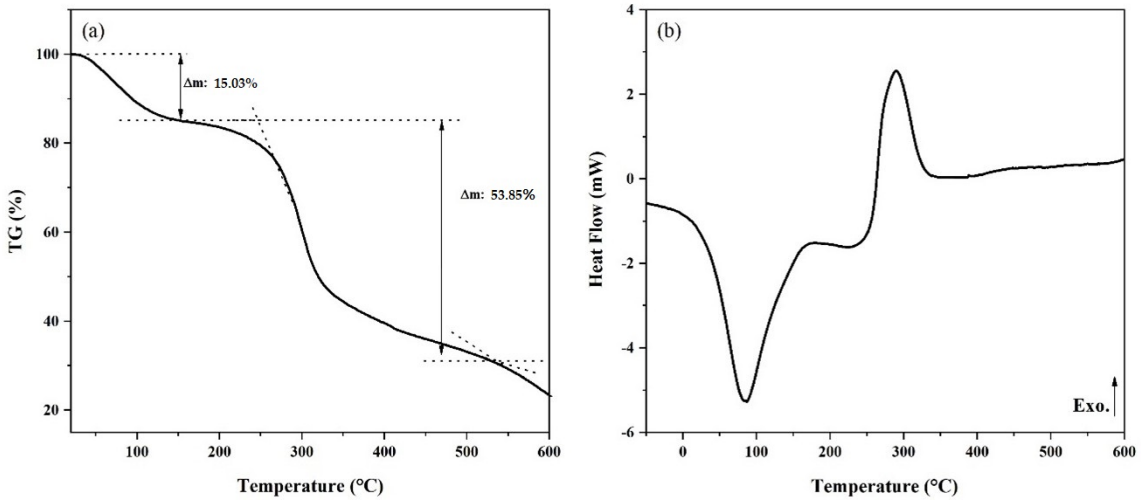

Figure 6. Thermal stability curves of GC blend: (**a**) TG and (**b**) DSC.

In Figure 5b, the endothermic event present in the range 20 to 100 °C, more precisely at 52.74 °C, corroborates the information given by the TG curve and can be attributed to the evaporation of adsorbed water [77]. In the range of 100–300 °C, a broad exothermic peak can be considered. This peak is due to crystal growth and lattice strain release during the heating process. In the grinding process, a large amount of strain and defects are incorporated into the powder particles and, when the milled sample is heated, grain growth takes place and strain is released, although no phase transformation occurs up to 1200 °C [72].

The thermogram of the GC blend, shown in Figure 6a, indicates that the thermal decomposition occurs in two stages. In the first, in the range of 25 to 150 °C, there is a loss of 15.03% of the initial mass of the sample resulting from the water release. In the second, between 200 and 350 °C, a pronounced decline in the TG curve is observed, referring to the disintegration of macromolecules related to the polymeric groups present in the blend as well as the decomposition of the organic material, which results in the loss of another 53.85% of the initial mass.

In Figure 6b, the thermal transitions present in the GC blend were verified through the DSC. The two events present in the thermogram are represented by two peaks, one endothermic at 85 °C and one exothermic at 290 °C, respectively. The endothermic peak is related to the loss of water in the structure and the exothermic peak with the degradation of the material. The GC blend can be considered thermally stable due to the presence of two well-defined thermal transition regions [68,72].

In the thermal analyses of the bioceramics H70GC30, H80GC20 and H90GC10, no divergences were observed with the results presented by HAP. This occurred since the biopolymers degraded at a temperature of around 290 °C; therefore, the bioceramics only show the presence of HAP, an outcome that can relate to the results obtained in the FTIR.

3.4. Morphological Analysis

The sample morphology was investigated using SEM. Figure 7 presents the micrographs of H70GC30, H80GC20 and H90GC10 bioceramics, with a magnification factor of 25,000×. The grains can be described as small spherical particles, being in consonance with the morphology presented by pure hydroxyapatite.

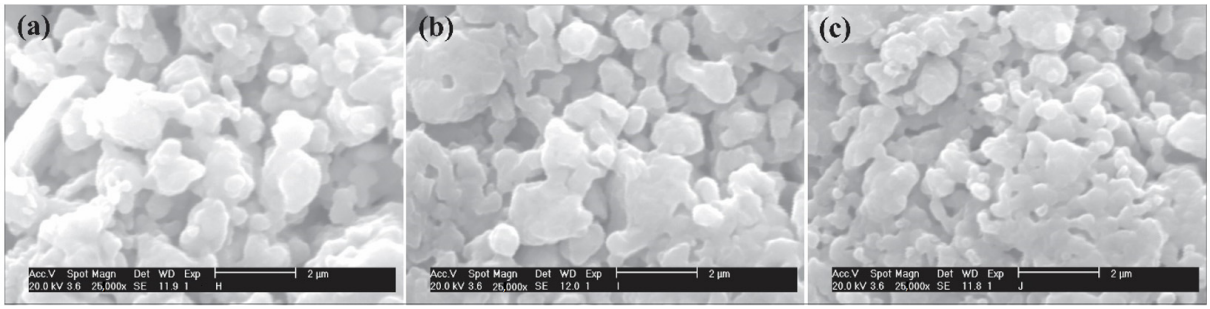

Figure 7. Micrographs of the sintered bioceramics: (**a**) H70GC30, (**b**) H80GC20 and (**c**) H90GC10.

Table 3 shows the average grain size, the experimental density and the Vickers hardness obtained for each sample. For the HAP, the average estimated grain size, 0.5 µm, is aligned with the values reported by Macêdo et al. [34]. It can be observed that the increase in the CG blend content promoted an increase in the average grain size. This grain growth has an impact on the porosity of the samples since a decrease in the experimental density can be observed.

Table 3. Average grain size, Vickers hardness and density of HAP, H70GC30, H80GC20 and H90GC10 bioceramics.

Bioceramics	Average Grain Size (µm)	Density (g/cm^3)	Vickers Hardness (GPa)
HAP	0.5	2.61	1.9
H70GC30	0.75	2.20	0.73
H80GC20	0.69	2.32	0.79
H90GC10	0.60	2.67	0.97

The Vickers hardness of HAP, H70GC30, H80GC20 and H90GC10 bioceramics was calculated with Equation (8). It is observed that the hardness of the bioceramics decreased with the biopolymer addition. This behavior was expected since the main contribution of the decrease of the microhardness is the decrease in the ceramic density [50].

3.5. Dielectric Spectroscopy

The dielectric behavior of the GC blend as a function of frequency is depicted in Figure 8. Figure 8a shows that the dielectric constant, ε', at room temperature and in the frequency range considered. This constant decreases monotonically with increasing

frequency. The continuous decrease of the dielectric constant with increasing frequency is a common behavior for all dielectric materials [78] and is due to the fact that when the frequency of the applied electric field increases, the mechanism of polarization will not be able to follow the change in the electric field and, therefore, the contribution of polarization to the dielectric constant will diminish [51,78,79]. At higher frequencies, when already in the limit of the measurement window, it is possible to infer that the ε' values tend to stabilize, a prediction supported by the dielectric behavior observed in several polymers [79]. Figure 8b presents the tangent loss, *tanδ*, as a function of the frequency. The inexistence of peaks shows that, at room temperature and in the frequency range of the measurements, the CG blend does not present any relaxation phenomenon and, since the values of *tanδ* are inferior to one, based on Equation (11), it is possible to conclude that the dielectric losses are inferior to the dielectric constant.

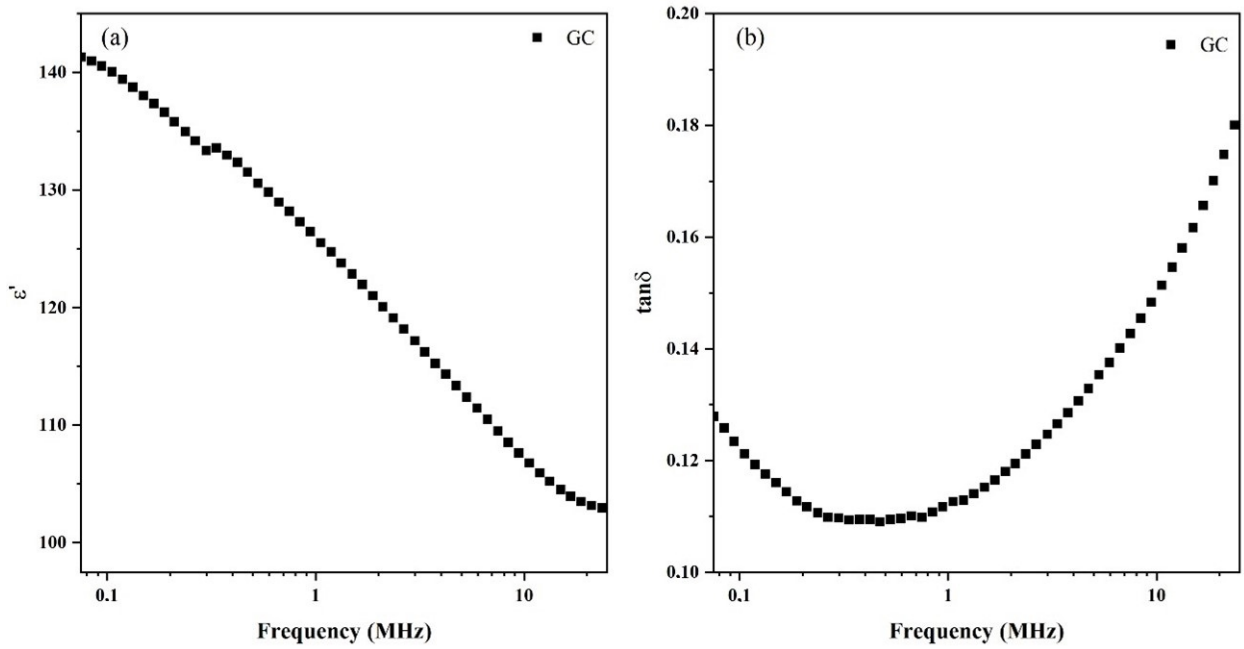

Figure 8. (**a**) ε' and (**b**) *tanδ* as a function of the frequency of the GC blend.

The dielectric properties of the bioceramics H70GC30, H80GC20 and H90GC10, depicted in Figure 9, are related to the different types of polarization present in the sample. The interfaces of bioceramics with biopolymers have a large number of defects that result in an unequal distribution of charges [80]. It can be verified in Figure 9a that the increase in the amount of GC promoted the increase of ε'. This enhancement in the dielectric constant values shows the increased energy storage capacity of the studied bioceramics [78–83]. With the addition of GC, cations are the dominant charges and may be responsible for the increase in the dielectric constant [34]. Until ≈ 10 MHz, the samples show a quasi-frequency independent behavior, indicating that the materials do not exhibit intense polarization processes and that the stored charge remains practically constant in the frequency range considered. At higher frequencies (>10 MHz), the charge carriers are unable to follow the rapid changes in the applied electric field and, as a consequence, the dielectric constant values start to decrease [81,82].

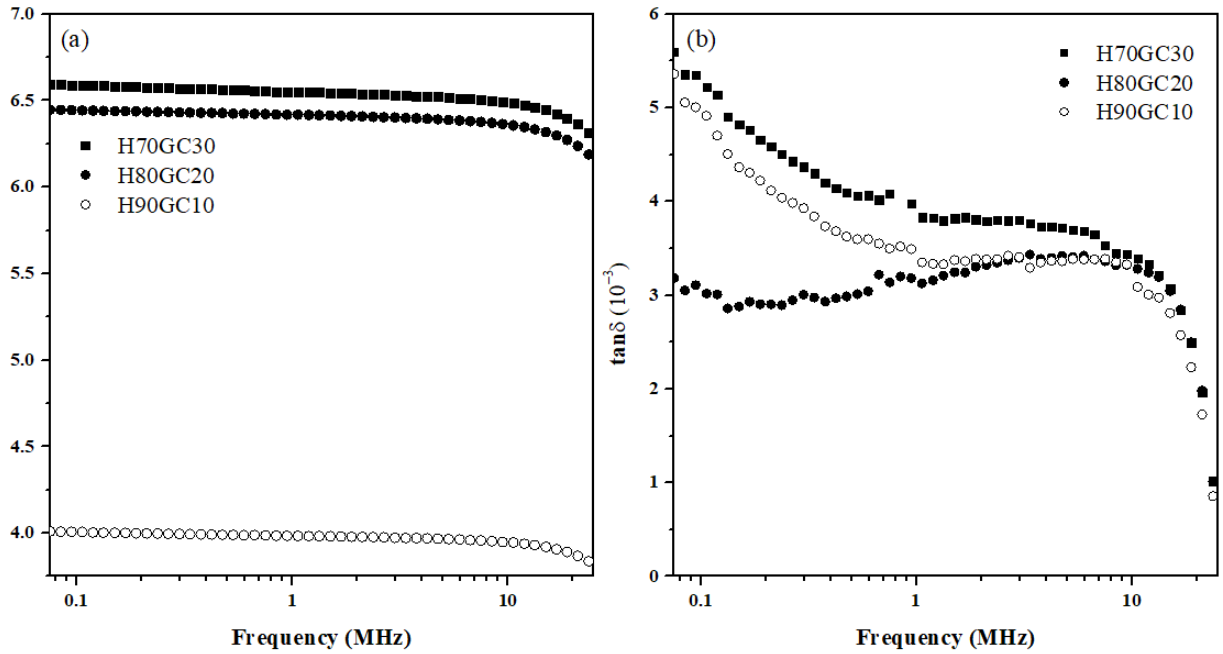

Figure 9. (**a**) ε' and (**b**) *tanδ* as a function of the frequency of H70GC30, H80GC20 and H90GC10 bioceramics.

Figure 9b presents the *tanδ* as a function of the frequency for the studied bioceramics. Since the *tanδ* values are inferior to one, the energy dissipated is inferior to the stored energy [84]. It is also noted that the highest dissipated energy is from bioceramics containing higher concentrations of biopolymer (H70GC30).

The dielectric properties of inorganic compounds containing galactomannan and chitosan have direct relationships with the concentration of the biopolymer [61,65,69,85].

4. Conclusions

Overall, the XRD pattern, Rietveld refinement and FTIR collectively indicated that the methodology of synthesis of HAP nanocrystalline powders was efficient, allowing us to obtain a single HAP phase. The FTIR spectrum showed that the GC blending process did not promote an alteration of the vibrational properties, presenting characteristic bands of galactomannan and chitosan.

Dielectric, morphological, hardness and density analyses confirmed that the GC blend, as well as its concentration, influenced the properties of the HAP. The dielectric analysis also showed a relationship between the concentration of the GC blend and the dielectric constant of the bioceramic since the blend favored the increase of ε' without compromising the *tanδ*, which presented values in the order of 10^{-3}.

Author Contributions: Conceptualization, E.d.S.G., M.P.F.G. and A.A.M.M.; methodology, E.d.S.G. and A.A.M.M.; software, S.R.G. and S.D.; validation, S.D., M.P.F.G. and A.A.M.M.; formal analysis, M.P.F.G. and A.A.M.M.; investigation, E.d.S.G., A.M.d.O.L., S.R.G. and S.D.; resources, S.D., M.P.F.G. and A.A.M.M.; data curation, A.A.M.M.; writing—original draft preparation, E.d.S.G.; writing—review and editing, S.R.G., S.D. and M.P.F.G.; visualization, A.M.d.O.L.; supervision, A.A.M.M.; project administration, A.A.M.M.; funding acquisition, M.P.F.G. All authors have read and agreed to the published version of the manuscript.

Funding: This research was funded by FEDER funds through the COMPETE 2020 Program and National Funds through FCT—Portuguese Foundation for Science and Technology—under the project LISBOA-01-0247-FEDER-039985/POCI-01-0247-FEDER-039985, LA/P/0037/2020, UIDP/50025/2020, and UIDB/50025/2020 of the Associate Laboratory Institute of Nanostructures, Nanomodelling and Nanofabrication—i3N. S.R. Gavinho acknowledges FCT—Portuguese Foundation for Science and Technology—for the PhD grant (SFRH/BD/148233/2019).

Institutional Review Board Statement: Not applicable.

Informed Consent Statement: Not applicable.

Data Availability Statement: The data presented in this study are available on request from the corresponding author.

Conflicts of Interest: The authors declare no conflict of interest.

References

1. Ragunathan, S.; Govindasamy, G.; Raghul, D.R.; Karuppaswamy, M.; Vijayachandra Togo, R.K. Hydroxyapatite reinforced natural polymer scaffold for bone tissue regeneration. *Mater. Today Proc.* **2020**, *23*, 111–118. [CrossRef]
2. Arvidson, K.; Abdallah, B.M.; Applegate, L.A.; Baldini, N.; Cenni, E.; Gomez-Barrena, E.; Granchi, D.; Kassem, M.; Konttinen, Y.T.; Mustafa, K.; et al. Bone regeneration and stem cells. *J. Cell. Mol. Med.* **2011**, *15*, 718–746. [CrossRef] [PubMed]
3. Kalita, S.J.; Bhardwaj, A.; Bhatt, H.A. Nanocrystalline calcium phosphate ceramics in biomedical engineering. *Mater. Sci. Eng. C* **2007**, *27*, 441–449. [CrossRef]
4. Daglilar, S.; Erkan, M.E. A study on bioceramic reinforced bone cements. *Mater. Lett.* **2007**, *61*, 1456–1459. [CrossRef]
5. Sadat-Shojai, M.; Khorasani, M.T.; Dinpanah-Khoshdargi, E.; Jamshidi, A. Synthesis methods for nanosized hydroxyapatite with diverse structures. *Acta Biomater.* **2013**, *9*, 7591–7621. [CrossRef]
6. Hwang, K.; Lim, Y. Chemical and structural changes of hydroxyapatite films by using a sol–gel method. *Surf. Coat. Technol.* **1999**, *115*, 172–175. [CrossRef]
7. Suchanek, W.L.; Byrappa, K.; Shuk, P.; Riman, R.E.; Janas, V.F.; Ten Huisen, K.S. Preparation of magnesium-substituted hydroxyapatite powders by the mechanochemical–hydrothermal method. *Biomaterials* **2004**, *25*, 4647–4657. [CrossRef]
8. Rigo, E.C.D.S.; Oliveira, L.C.; Santos, L.A.; Boschi, A.O.; Carrodeguas, R.G. Implantes metálicos recobertos com hidroxiapatita. *Res. Biomed. Eng.* **1999**, *15*, 21–29.
9. Assis, C.M.D.; Vercik, L.C.D.O.; Santos, M.L.D.; Fook, M.V.L.; Guastaldi, A.C. Comparison of crystallinity between natural hydroxyapatite and synthetic cp-Ti/HA coatings. *Mater. Res.* **2005**, *8*, 207–211. [CrossRef]
10. Nikpour, M.R.; Rabiee, S.M.; Jahanshahi, M.J.C.P.B.E. Synthesis and characterization of hydroxyapatite/chitosan nanocomposite materials for medical engineering applications. *Compos. Part B* **2012**, *43*, 1881–1886. [CrossRef]
11. Silva, C.C.; Valente, M.A.; Graça, M.P.F.; Sombra, A.S.B. Preparation and optical characterization of hydroxyapatite and ceramic systems with titanium and zirconium formed by dry high-energy mechanical alloying. *Solid State Sci.* **2004**, *6*, 1365–1374. [CrossRef]
12. Motskin, M.; Wright, D.M.; Muller, K.; Kyle, N.; Gard, T.G.; Porter, A.E.; Skepper, J.N. Hydroxyapatite nano and microparticles: Correlation of particle properties with cytotoxicity and biostability. *Biomaterials* **2009**, *30*, 3307–3317. [CrossRef] [PubMed]
13. Wang, S.; Kempen, D.H.; Yaszemski, M.J.; Lu, L. The roles of matrix polymer crystallinity and hydroxyapatite nanoparticles in modulating material properties of photo-crosslinked composites and bone marrow stromal cell responses. *Biomaterials* **2009**, *30*, 3359–3370. [CrossRef] [PubMed]
14. Mohandes, F.; Salavati-Niasari, M.; Fathi, M.; Fereshteh, Z. Hydroxyapatite nanocrystals: Simple preparation, characterization and formation mechanism. *Mater. Sci. Eng. C* **2014**, *45*, 29–36. [CrossRef]
15. Yasukawa, A.; Kandori, K.; Tanaka, H.; Gotoh, K. Preparation and structure of carbonated calcium hydroxyapatite substituted with heavy rare earth ions. *Mater. Res. Bull.* **2012**, *47*, 1257–1263. [CrossRef]
16. Yasukawa, A.; Gotoh, K.; Tanaka, H.; Kandori, K. Preparation and structure of calcium hydroxyapatite substituted with light rare earth ions. *Colloids Surf. A* **2012**, *393*, 53–59. [CrossRef]
17. Kaygili, O.; Dorozhkin, S.V.; Ates, T.; Al-Ghamdi, A.A.; Yakuphanoglu, F. Dielectric properties of Fe doped hydroxyapatite prepared by sol–gel method. *Ceram. Int.* **2014**, *40*, 9395–9402. [CrossRef]
18. Zhang, W.; Cao, N.; Chai, Y.; Xu, X.; Wang, Y. Synthesis of nanosize single-crystal strontium hydroxyapatite via a simple sol–gel method. *Ceram. Int.* **2014**, *40*, 16061–16064. [CrossRef]
19. Silva, C.C.; Graça, M.P.F.; Valente, M.A.; Sombra, A.S.B. Structural study of Fe_2O_3-doped calcium phosphates obtained by the mechanical milling method. *Phys. Scr.* **2009**, *79*, 055601. [CrossRef]
20. Nasiri-Tabrizi, B.; Fahami, A.; Ebrahimi-Kahrizsangi, R. Effect of milling parameters on the formation of nanocrystalline hydroxyapatite using different raw materials. *Ceram. Inter.* **2013**, *39*, 5751–5763. [CrossRef]
21. Rhee, S.H. Synthesis of hydroxyapatite via mechanochemical treatment. *Biomaterials* **2002**, *23*, 1147–1152. [CrossRef] [PubMed]
22. Cho, J.S.; Rhee, S.H. Formation mechanism of nano-sized hydroxyapatite powders through spray pyrolysis of a calcium phosphate solution containing polyethylene glycol. *J. Eur. Ceram. Soc.* **2013**, *33*, 233–241. [CrossRef]
23. Liu, H.S.; Chin, T.S.; Lai, L.S.; Chiu, S.Y.; Chung, K.H.; Chang, C.S.; Lui, M.T. Hydroxyapatite synthesized by a simplified hydrothermal method. *Ceram. Inter.* **1997**, *23*, 19–25. [CrossRef]
24. Lala, S.; Satpati, B.; Kar, T.; Pradhan, S.K. Structural and microstructural characterizations of nanocrystalline hydroxyapatite synthesized by mechanical alloying. *Mater. Sci. Eng. C* **2013**, *33*, 2891–2898. [CrossRef] [PubMed]

25. Macuvele, D.L.P.; Nones, J.; Matsinhe, J.V.; Lima, M.M.; Soares, C.; Fiori, M.A.; Riella, H.G. Advances in ultra high molecular weight polyethylene/hydroxyapatite composites for biomedical applications: A brief review. *Mater. Sci. Eng. C* **2017**, *76*, 1248–1262. [CrossRef] [PubMed]
26. Chen, F.; Wang, Z.C.; Lin, C.J. Preparation and characterization of nano-sized hydroxyapatite particles and hydroxyapatite/chitosan nano-composite for use in biomedical materials. *Mater. Lett.* **2002**, *57*, 858–861. [CrossRef]
27. Zhang, L.J.; Feng, X.S.; Liu, H.G.; Qian, D.J.; Zhang, L.; Yu, X.L.; Cui, F.Z. Hydroxyapatite/collagen composite materials formation in simulated body fluid environment. *Mater. Lett.* **2004**, *58*, 719–722. [CrossRef]
28. Maeda, Y.; Jayakumar, R.; Nagahama, H.; Furuike, T.; Tamura, H. Synthesis, characterization and bioactivity studies of novel β-chitin scaffolds for tissue-engineering applications. *Int. J. Biol. Macromol.* **2008**, *42*, 463–467. [CrossRef]
29. Manara, S.; Paolucci, F.; Palazzo, B.; Marcaccio, M.; Foresti, E.; Tosi, G.; Sabbatini, S.; Sabatino, P.; Altankov, G.; Roveri, N. Electrochemically-assisted deposition of biomimetic hydroxyapatite–collagen coatings on titanium plate. *Inorg. Chim. Acta* **2008**, *361*, 1634–1645. [CrossRef]
30. Madhumathi, K.; Shalumon, K.T.; Rani, V.D.; Tamura, H.; Furuike, T.; Selvamurugan, N.; Nair, S.V.; Jayakumar, R. Wet chemical synthesis of chitosan hydrogel–hydroxyapatite composite membranes for tissue engineering applications. *Int. J. Biol. Macromol.* **2009**, *45*, 12–15. [CrossRef]
31. Pang, X.; Casagrande, T.; Zhitomirsky, I. Electrophoretic deposition of hydroxyapatite–CaSiO3–chitosan composite coatings. *J. Colloid Interface Sci.* **2009**, *330*, 323–329. [CrossRef] [PubMed]
32. Trakoolwannachai, V.; Kheolamai, P.; Ummartyotin, S. Development of hydroxyapatite from eggshell waste and a chitosan-based composite: In vitro behavior of human osteoblast-like cell (Saos-2) cultures. *Int. J. Biol. Macromol.* **2019**, *134*, 557–564. [CrossRef] [PubMed]
33. Pereira, M.B.B.; França, D.B.; Araújo, R.C.; Silva Filho, E.C.; Rigaud, B.; Fonseca, M.G.; Jaber, M. Amino hydroxyapatite/chitosan hybrids reticulated with glutaraldehyde at different pH values and their use for diclofenac removal. *Carbohydr. Polym.* **2020**, *236*, 116036. [CrossRef] [PubMed]
34. Macêdo, A.A.M.; Sombra, A.S.B.; Mazzetto, S.E.; Silva, C.C. Influence of the polysaccharide galactomannan on the dielectrical characterization of hydroxyapatite ceramic. *Compos. Part B* **2013**, *44*, 95–99. [CrossRef]
35. Pawlik, A.; Rehman, M.A.U.; Nawaz, Q.; Bastan, F.E.; Sulka, G.D.; Boccaccini, A.R. Fabrication and characterization of electrophoretically deposited chitosan-hydroxyapatite composite coatings on anodic titanium dioxide layers. *Electrochim. Acta* **2019**, *307*, 465–473. [CrossRef]
36. Cunha, C.S.; Castro, P.J.; Sousa, S.C.; Pullar, R.C.; Tobaldi, D.M.; Piccirillo, C.; Pintado, M.M. Films of chitosan and natural modified hydroxyapatite as effective UV-protecting, biocompatible and antibacterial wound dressings. *Int. J. Biol. Macromol.* **2020**, *159*, 1177–1185. [CrossRef]
37. Olivera, S.; Muralidhara, H.B.; Venkatesh, K.; Guna, V.K.; Gopalakrishna, K.; Kumar, Y. Potential applications of cellulose and chitosan nanoparticles/composites in wastewater treatment: A review. *Carbohydr. Polym.* **2016**, *153*, 600–618. [CrossRef]
38. Croisier, F.; Jérôme, C. Chitosan-based biomaterials for tissue engineering. *Eur. Polym. J.* **2013**, *49*, 780–792. [CrossRef]
39. Thanyacharoen, T.; Chuysinuan, P.; Techasakul, S.; Noenplab, A.N.L.; Ummartyotin, S. The chemical composition and antioxidant and release properties of a black rice (Oryza sativa L.)-loaded chitosan and polyvinyl alcohol composite. *J. Mol. Liq.* **2017**, *248*, 1065–1070. [CrossRef]
40. Thanyacharoen, T.; Chuysinuan, P.; Techasakul, S.; Nooeaid, P.; Ummartyotin, S. Development of a gallic acid-loaded chitosan and polyvinyl alcohol hydrogel composite: Release characteristics and antioxidant activity. *Int. J. Biol. Macromol.* **2018**, *107*, 363–370. [CrossRef]
41. Kök, M.S.; Hill, S.E.; Mitchell, J.R. Viscosity of galactomannans during high temperature processing: Influence of degradation and solubilisation. *Food Hydrocoll.* **1999**, *13*, 535–542. [CrossRef]
42. Fernandes, P.B.; Gonçalves, M.P.; Doublier, J.L. A rheological characterization of kappa-carrageenan/galactomannan mixed gels: A comparison of locust bean gum samples. *Carbohydr. Polym.* **1991**, *16*, 253–274. [CrossRef]
43. Bresolin, T.M.B.; Milas, M.; Rinaudo, M.; Reicher, F.; Ganter, J.L.M.S. Role of galactomannan composition on the binary gel formation with xanthan. *Int. J. Biol. Macromol.* **1999**, *26*, 225–231. [CrossRef] [PubMed]
44. Vendruscolo, C.W.; Andreazza, I.F.; Ganter, J.L.M.S.; Ferrero, C.; Bresolin, T.M.B. Xanthan and galactomannan (from M. scabrella) matrix tablets for oral controlled delivery of theophylline. *Int. J. Pharm.* **2005**, *296*, 1–11. [CrossRef]
45. Rietveld, H.M. Line profiles of neutron powder-diffraction peaks for structure refinement. *Acta Crystallogr.* **1967**, *22*, 151–152. [CrossRef]
46. Doebelin, N.; Kleeberg, R. Profex: A graphical user interface for the Rietveld refinement program BGMN. *J. Appl. Crystallogr.* **2015**, *48*, 1573–1580. [CrossRef]
47. Hayakawa, S.; Li, Y.; Tsuru, K.; Osaka, A.; Fujii, E.; Kawabata, K. Preparation of nanometer-scale rod array of hydroxyapatite crystal. *Acta Biomater.* **2009**, *5*, 2152–2160. [CrossRef]
48. Vinodhini, P.A.; Sangeetha, K.; Thandapani, G.; Sudha, P.N.; Jayachandran, V.; Sukumaran, A. FTIR, XRD and DSC studies of nanochitosan, cellulose acetate and polyethylene glycol blend ultrafiltration membranes. *Int. J. Biol. Macromol.* **2017**, *104*, 1721–1729. [CrossRef]
49. Hoepfner, T.P.; Case, E.D. The influence of the microstructure on the hardness of sintered hydroxyapatite. *Ceram. Int.* **2003**, *29*, 699–706. [CrossRef]

50. Pinto Filho, F.; Nogueira, R.E.F.Q.; Graça, M.P.F.; Valente, M.A.; Sombra, A.S.B.; Silva, C.C.D. Structural and mechanical study of the sintering effect in hydroxyapatite doped with iron oxide. *Physica B* **2008**, *403*, 3826–3829. [CrossRef]
51. Figueiró, S.D.; Macêdo, A.A.M.; Melo, M.R.S.; Freitas, A.L.P.; Moreira, R.A.; De Oliveira, R.S.; Goés, J.C.; Sombra, A.S.B. On the dielectric behaviour of collagen–algal sulfated polysaccharide blends: Effect of glutaraldehyde crosslinking. *Biophys. Chem.* **2006**, *120*, 154–159. [CrossRef] [PubMed]
52. Peixoto, M.V.; Costa, F.M.; Devesa, S.; Graça, M.P.F. Structural, Morphological and Dielectric Characterization of $BiFeO_3$ Fibers Grown by the LFZ Technique. *Crystals* **2023**, *13*, 960. [CrossRef]
53. Ashoorirad, M.; Saviz, M.; Fallah, A. On the electrical properties of collagen macromolecule solutions: Role of collagen-water interactions. *J. Mol. Liq.* **2020**, *300*, 112344. [CrossRef]
54. Salema, A.A.; Yeow, Y.K.; Ishaque, K.; Ani, F.N.; Afzal, M.T.; Hassan, A. Dielectric properties and microwave heating of oil palm biomass and biochar. *Ind. Crops Prod.* **2013**, *50*, 366–374. [CrossRef]
55. Dorey, R. Microstructure–property relationships: How the microstructure of the film affects its properties. In *Ceramic Thick Films for MEMS and Microdevices*; Dorey, R., Ed.; William Andrew Publishing: Norwich, NY, USA, 2012; pp. 85–112. [CrossRef]
56. Graça, M.P.F.; da Silva, M.F.; Valente, M.A. $NaNbO_3$ crystals dispersed in a B_2O_3 glass matrix–Structural characteristics versus electrical and dielectrical properties. *Solid State Sci.* **2009**, *11*, 570–577. [CrossRef]
57. Kazin, P.E.; Pogosova, M.A.; Trusov, L.A.; Kolesnik, I.V.; Magdysyuk, O.V.; Dinnebier, R.E. Crystal structure details of La-and Bi-substituted hydroxyapatites: Evidence for LaO^+ and BiO^+ with a very short metal–oxygen bond. *J. Solid State Chem.* **2016**, *237*, 349–357. [CrossRef]
58. Silva, C.C.; Pinheiro, A.G.; Miranda, M.A.R.; Góes, J.C.; Sombra, A.S.B. Structural properties of hydroxyapatite obtained by mechanosynthesis. *Solid State Sci.* **2013**, *5*, 553–558. [CrossRef]
59. Sarkar, A.; Kannan, S. In situ synthesis, fabrication and Rietveld refinement of the hydroxyapatite/titania composite coatings on 316 L SS. *Ceram. Int.* **2014**, *40*, 6453–6463. [CrossRef]
60. Bhadang, K.A.; Gross, K.A. Influence of fluorapatite on the properties of thermally sprayed hydroxyapatite coatings. *Biomaterials* **2004**, *25*, 4935–4945. [CrossRef]
61. Silva, C.C.D.; Rocha, H.H.B.; Freire, F.N.A.; Santos, M.R.P.; Sabóia, K.D.A.; Góes, J.C.; Sombra, A.S.B. Hydroxyapatite screen-printed thick films: Optical and electrical properties. *Mater. Chem. Phys.* **2005**, *92*, 260–268. [CrossRef]
62. Sanosh, K.P.; Chu, M.C.; Balakrishnan, A.; Lee, Y.J.; Kim, T.N.; Cho, S.J. Synthesis of nano hydroxyapatite powder that simulate teeth particle morphology and composition. *Curr. Appl. Phys.* **2009**, *9*, 1459–1462. [CrossRef]
63. Xia, Z.; Liao, L.; Zhao, S. Synthesis of mesoporous hydroxyapatite using a modified hard-templating route. *Mater. Res. Bull.* **2009**, *44*, 1626–1629. [CrossRef]
64. Yang, P.; Quan, Z.; Li, C.; Kang, X.; Lian, H.; Lin, J. Bioactive, luminescent and mesoporous europium-doped hydroxyapatite as a drug carrier. *Biomaterials* **2008**, *29*, 4341–4347. [CrossRef]
65. Wang, J.; Somasundaran, P. Study of galactomannose interaction with solids using AFM, IR and allied techniques. *J. Colloid Interface Sci.* **2007**, *309*, 373–383. [CrossRef] [PubMed]
66. Tang, E.S.K.; Huang, M.; Lim, L.Y. Ultrasonication of chitosan and chitosan nanoparticles. *Int. J. Pharm* **2003**, *265*, 103–114. [CrossRef]
67. Ding, W.; Lian, Q.; Samuels, R.J.; Polk, M.B. Synthesis and characterization of a novel derivative of chitosan. *Polymer* **2003**, *44*, 547–556. [CrossRef]
68. Govindan, S.; Nivethaa, E.A.K.; Saravanan, R.; Narayanan, V.; Stephen, A. Synthesis and characterization of chitosan–silver nanocomposite. *Appl. Nanosci.* **2012**, *2*, 299–303. [CrossRef]
69. Lima, C.G.A.; De Oliveira, R.S.; Figueiró, S.D.; Wehmann, C.F.; Góes, J.C.; Sombra, A.S.B. DC conductivity and dielectric permittivity of collagen–chitosan films. *Mater. Chem. Phys.* **2016**, *99*, 284–288. [CrossRef]
70. Figueiró, S.D.; Góes, J.C.; Moreira, R.A.; Sombra, A.S.B. On the physico-chemical and dielectric properties of glutaraldehyde crosslinked galactomannan–collagen films. *Carbohydr. Polym.* **2004**, *56*, 313–320. [CrossRef]
71. Park, S.H.; Chun, M.K.; Choi, H.K. Preparation of an extended-release matrix tablet using chitosan/Carbopol interpolymer complex. *Int. J. Pharm.* **2018**, *347*, 39–44. [CrossRef]
72. Mandal, T.; Mishra, B.K.; Garg, A.; Chaira, D. Optimization of milling parameters for the mechanosynthesis of nanocrystalline hydroxyapatite. *Powder Technol.* **2014**, *253*, 650–656. [CrossRef]
73. Bulina, N.V.; Makarova, S.V.; Baev, S.G.; Matvienko, A.A.; Gerasimov, K.B.; Logutenko, O.A.; Bystrov, V.S. A study of thermal stability of hydroxyapatite. *Minerals* **2021**, *11*, 1310. [CrossRef]
74. Tonsuaadu, K.; Gross, K.A.; Plūduma, L.; Veiderma, M. A review on the thermal stability of calcium apatites. *J. Therm. Anal. Calorim.* **2012**, *110*, 647–659. [CrossRef]
75. Wang, T.; Dorner-Reisel, A.; Müller, E. Thermogravimetric and thermokinetic investigation of the dehydroxylation of a hydroxyapatite powder. *J. Eur. Ceram. Soc.* **2004**, *24*, 693–698. [CrossRef]
76. Mostafa, N.Y. Characterization, thermal stability and sintering of hydroxyapatite powders prepared by different routes. *Mater. Chem. Phys.* **2005**, *94*, 333–341. [CrossRef]
77. Zima, A. Hydroxyapatite-chitosan based bioactive hybrid biomaterials with improved mechanical strength. *Spectrochim. Acta Part A* **2018**, *193*, 175–184. [CrossRef]

78. Rahman, P.M.; Mujeeb, V.A.; Muraleedharan, K.; Thomas, S.K. Chitosan/nano ZnO composite films: Enhanced mechanical, antimicrobial and dielectric properties. *Arabian J. Chem.* **2018**, *11*, 120–127. [CrossRef]
79. Raja, V.; Sharma, A.K.; Rao, V.N. Impedance spectroscopic and dielectric analysis of PMMA-CO-P4VPNO polymer films. *Mater. Lett.* **2004**, *58*, 3242–3247. [CrossRef]
80. Bonardd, S.; Robles, E.; Barandiaran, I.; Saldías, C.; Leiva, Á.; Kortaberria, G. Biocomposites with increased dielectric constant based on chitosan and nitrile-modified cellulose nanocrystals. *Carbohydr. Polym.* **2018**, *199*, 20–30. [CrossRef]
81. Al-Muntaser, A.A.; Pashameah, R.A.; Alzahrani, E.; AlSubhi, S.A.; Hameed, S.T.; Morsi, M.A. Graphene nanoplatelets/TiO_2 hybrid nanofiller boosted PVA/CMC blend based high performance nanocomposites for flexible energy storage applications. *J. Polym. Environ.* **2023**, *31*, 2534–2548. [CrossRef]
82. El-Naggar, A.M.; Heiba, Z.K.; Kamal, A.M.; Alzahrani, K.E.; Abd-Elkader, O.H.; Mohamed, M.B. Impact of natural melanin doping on the structural, optical and dielectric characteristics of the PVP/CMC blend. *J. Taibah Univ. Sci.* **2023**, *17*, 2190731. [CrossRef]
83. Abdullah, A.Q.; Ali, N.A.; Hussein, S.I.; Hakamy, A.; Abd-Elnaiem, A.M. Improving the Dielectric, Thermal, and Electrical Properties of Poly (Methyl Methacrylate)/Hydroxyapatite Blends by Incorporating Graphene Nanoplatelets. *J. Inorg. Organomet. Polym. Mater.* **2023**, 1–12. [CrossRef]
84. Bhatt, A.S.; Bhat, D.K.; Santosh, M.S. Electrical and magnetic properties of chitosan-magnetite nanocomposites. *Physica B* **2010**, *405*, 2078–2082. [CrossRef]
85. Costa, M.M.; Sohn, R.S.T.M.; Macêdo, A.A.M.; Mazzetto, S.E.; Graça, M.P.F.; Sombra, A.S.B. Study of the temperature and organic bindings effects in the dielectric and structural properties of the lithium ferrite ceramic matrix ($LiFe_5O_8$). *J. Alloys Compd.* **2011**, *509*, 9466–9471. [CrossRef]